Editors' Suggestion

Inverse Orbital Torque via Spin-Orbital Intertwined States

E. Santos,[1] J.E. Abrão,[1] Dongwook Go,[2,3] L.K. de Assis,[4] Yuriy Mokrousov,[2,3] J.B.S. Mendes,[5] and A. Azevedo[1,*]

[1] *Departamento de Física, Universidade Federal de Pernambuco, Recife, Pernambuco 50670-901, Brazil*

[2] *Peter Grünberg Institut and Institute for Advanced Simulation, Forschungszentrum Jülich and JARA, 52425 Jülich, Germany*

[3] *Institute of Physics, Johannes Gutenberg University Mainz, 55099 Mainz, Germany*

[4] *Universidade Federal de Pernambuco, Programa de Pós-Graduação em Ciências dos Materiais, Recife, Pernambuco 50740-560, Brazil*

[5] *Departamento de Física, Universidade Federal de Viçosa, 36570-900 Viçosa, Minas Gerais, Brazil*

(Received 5 April 2022; revised 3 October 2022; accepted 20 December 2022; published 27 January 2023)

While current-induced torque by orbital current has been experimentally found in various structures, evidence for its reciprocity has been missing so far. Here, we report experimental evidence of strong inverse orbital torque in YIG/Pt/CuO_x (YIG = $Y_3Fe_5O_{12}$) mediated by spin-orbital mixed electronic states in Pt. By injecting spin current from YIG to Pt by the spin pumping via ferromagnetic resonance and by the spin Seebeck effect, we find a pronounced inverse spin Hall effectlike signal. While a part of the signal is explained as being due to the inverse spin-orbital Hall effect in Pt, we also find a substantial increase of the signal in YIG/Pt/CuO_x structures compared to the signal in YIG/Pt. We attribute this to the inverse orbital Rashba-Edelstein effect at the Pt/CuO_x interface mediated by the spin-orbital coupled states in Pt. Our work paves the way toward understanding of spin-orbital intertwined physics in nonequilibrium and provides a way for electrical detection of the orbital current in orbitronic device applications.

DOI: 10.1103/PhysRevApplied.19.014069

In the age of information technology, spin-based electronics has found wide application in data storage and processing. This field is facing increasing challenges that demand increasingly efficient materials for generation and manipulation of spin currents [1,2]. It turned out that spin-orbit coupling (SOC) enables generation of nonequilibrium spin accumulation, e.g., by the spin Hall effect (SHE) [3–5] and Rashba-Edelstein effect [6–9]. A reciprocal effect such as inverse SHE (ISHE) provides a way to detect spin current electrically. Injection of the SOC-induced spin to a ferromagnet can exert torque on the magnetization, which is known as spin-orbit torque (SOT), an effect that originates from the exchange interaction between nonequilibrium spins and local magnetic moments [10–12]. Since SOC increases with the atomic number, heavy metals, such as Pt, Ta, and W, have been widely used in spintronics investigation, making them prime candidates for devices used to manipulate the magnetization by electrical means only. In this scenario, light materials, such as Cu, are often overlooked, because they have negligible SOC.

However, recent studies have shown that naturally oxidized Cu films can significantly enhance SOT efficiency, which reveals a crucial role of an oxide interface [13–16]. This effect can be explained in the recently developed framework of orbital-angular-momentum (OAM) currents, which can be generated even in weak SOC materials. Apparently, OAM would not play any significant role due to the angular-momentum quenching in solids, however, it has been shown that the orbital Hall effect (OHE) can generate an OAM current in a transverse direction to an external electric field even if the OAM is completely quenched in the ground state [17–21]. At surfaces and interfaces, where the inversion symmetry is broken, orbital hybridizations induce a local electric dipole, which influences the OAM polarization. Its interaction with structural asymmetry results in the orbital Rashba effect (ORE) [22–27], which induces a chiral OAM texture for electronic states in k space. Thus, application of an external electric field can result in nonequilibrium OAM accumulation, which is known as the orbital Rashba-Edelstein effect (OREE) [27,28]—the orbital counterpart of the spin Rashba-Edelstein effect [6–8]. The transfer of the OAM to the magnetization of a magnetic material provides an alternative mechanism to induce magnetization dynamics [29].

*antonio.azevedo@ufpe.br

Such orbital torques (OTs) provide a promising route for magnetic nanodevices based on light elements.

Among different material candidates, a surface-oxidized Cu (CuO_x) is found to exhibit a strong OREE [27]. This is supported by recent papers on OT in heterostructures involving CuO_x [27,29,30]. In particular, Ref. [29] demonstrated an innovative route to achieve large torque efficiency using strong SOC of Pt in TIG/Pt/CuO_x structure, where TIG $= Tm_3Fe_5O_{12}$. In Ref. [29], the OAM induced by the OREE is harnessed by the orbital-to-spin conversion in Pt, which has strong SOC, and the resulting spin exerts torque on the magnetization of TIG. So far, we emphasize that there is still no experimental evidence of its reciprocal process, the inverse OT. We also note that Refs. [16,31] found negligible efficiency for the inverse OT.

In this paper, we report an experimental observation of the inverse OT in heterostructures of YIG(40)/Pt(t_{Pt})/CuO_x(3) by means of spin pumping via ferromagnetic resonance (FMR) and longitudinal spin Seebeck effect (LSSE) in YIG, where the numbers in parentheses indicate the thickness of each layer in nanometers. When comparing with the result in YIG(40)/Pt(t_{Pt}), we find a substantial increase of the inverse SHE-like signal upon adding a CuO_x capping layer, suggesting the crucial role of the Pt/CuO_x interface, where strong ORE exists. From this, we conclude that upon spin injection, nonequilibrium electronic states exhibit strong coupling between the spin and orbital due to the strong SOC of Pt, and it is converted into charge current by the inverse OREE (IOREE) at the Pt/CuO_x interface. The efficiency of this process depends on two aspects: (1) the spin-orbital degree of coupling that determines how efficiently the orbital current is conducted upward; (2) how strong is the IOREE, which is driven by the perpendicular E field (due to the inversion symmetry breaking and/or any charge-transfer process due to the oxidation) at the Pt/CuO_x interface. Figure 1 presents a schematic illustration of the mechanism for converting spin-orbital mixed current into charge current by two mechanisms. The spin is injected from YIG and as the spin couples with the OAM at Pt, it is converted into a charge current not only by the inverse SHE-OHE in Pt [Fig. 1(a)] but also via the IOREE at the CuO_x interface [Figs. 1(b) and 1(c)]. We find that this contribution is much stronger than the "conventional" contribution by the ISHE in Pt. Our finding not only demonstrates the inverse OT unambiguously, but also sheds light on the nonequilibrium spin-orbit physics. The YIG(40) film used in this work is grown by liquid phase epitaxy onto a 0.5-mm-thick (111)-oriented $Gd_3Ga_5O_{12}$ (GGG). The Pt and Cu films are dc-sputter-deposited at room temperature in a working pressure of 2.8 mTorr and a base pressure of 2.0×10^{-7} Torr or lower. The set of samples with the Cu capping layer is left outside the chamber for 2 days to naturally oxidize. All the YIG samples are cut from the same YIG(40) film in pieces with lateral dimensions of 1.5×3.0 mm^2 (see Appendix A for details).

The investigation of the structural properties of the heterostructures is carried out by conventional x-ray diffraction (XRD), grazing incidence x-ray diffraction (GIXRD), and SEM images. To investigate the oxidation process, we deposit a thick film of Cu(60) on top of the Pt(3) layer and left the sample exposed to air. The GIXRD pattern in Fig. 2(a) clearly shows the diffraction peaks characteristic of CuO_x and of the polycrystalline Cu film with preferential texture oriented along the planes (111), (200), (220), and (202), as previously reported [32]. We deposit a capping layer of Pt(5) on the Cu surface and the GIXRD pattern is shown in Fig. 2(b) where no CuO_x peaks are identified. Clearly the capping layer of Pt(5) prevents the

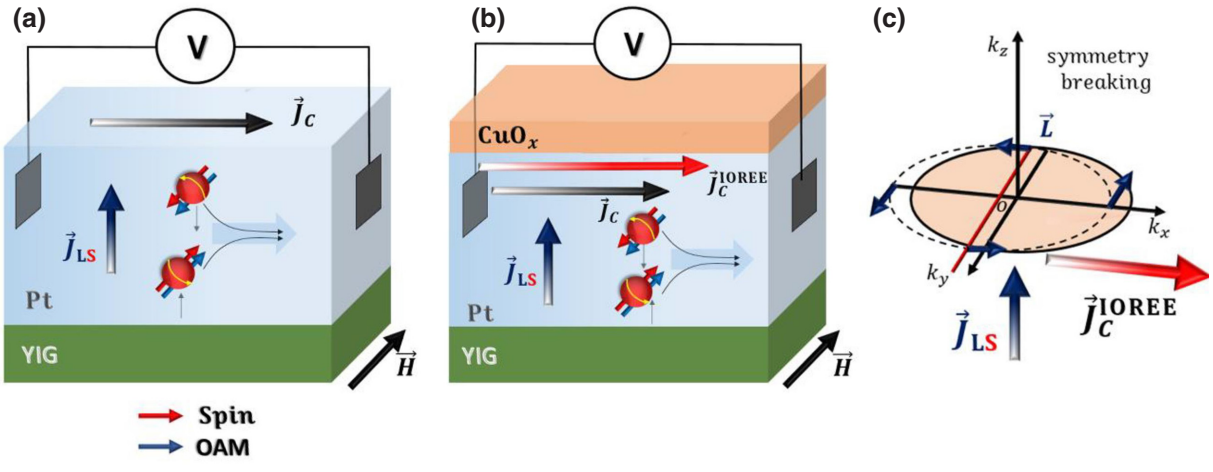

FIG. 1. Illustration of the inverse SHE and OHE process. (a) Without CuO_x layer, the only contribution is due to the conversion of $\vec{J}_{LS}$ in charge current. (b) With CuO_x layer, the additional $\vec{J}_C^{IOREE}$ appears driven by the interface Pt/CuO_x. (c) IOREE in the presence of a chiral OAM texture in k space.

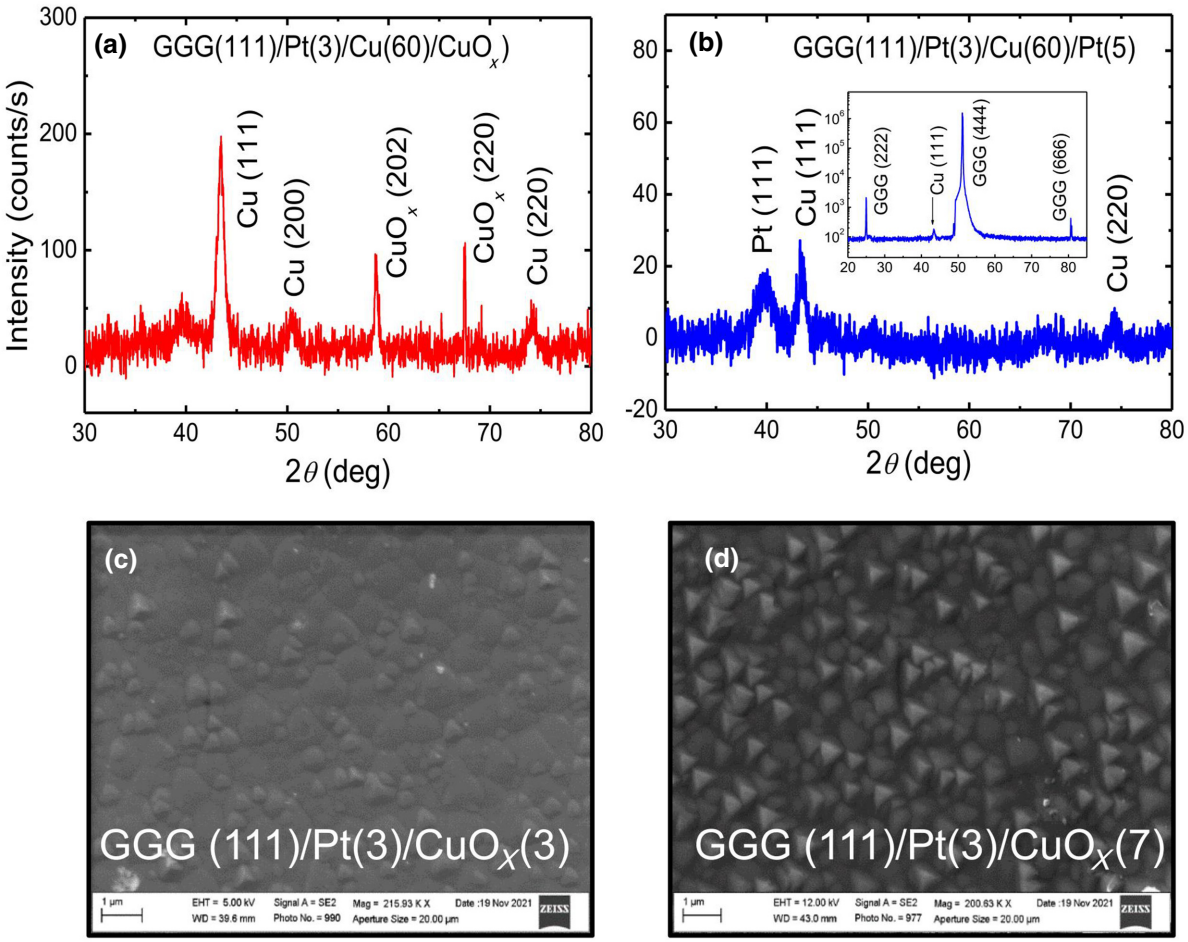

FIG. 2. (a) Shows the GIXRD pattern of a film of Cu(60) that is left in contact with air for 2 days. The result shows the presence of strong CuO_x peaks. In (b), the GIXRD pattern clearly shows that a capping layer of Pt(5) prevents the Cu layer oxidation. (c),(d) SEM surface images of $CuO_x(3)$ and $CuO_x(7)$, respectively. The images reveal pyramidal structures associated to the orientation of the GGG substrate. Inset of (b) shows the conventional XRD pattern of GGG/Pt(3)/Cu(60)/CuO_x, exhibiting reflections associated with the (222), (444), and (666) crystal planes of GGG as well as (111) texture of the Cu layer.

Cu oxidation. The XRD spectrum also shows the peak corresponding to (111) Bragg reflections from the Cu film, demonstrating that the orientation of the GGG substrate strongly influences the orientation of the Cu grains. Figures 2(c) and 2(d) show SEM images of Cu/CuO_x films deposited in GGG(111)/Pt(3) revealing a continuous film with different shapes of CuO_x pyramids with dimensions smaller than 1 μm associated to the orientation of the GGG substrate. Furthermore, preliminary results performed by TEM, on the samples used in this work, confirm that the natural oxidation of surface layers of Cu films can have thicknesses of up to approximately 10 nm.

We use the FMR-driven spin-pumping (FMR SP) technique excited at 9.41 GHz [33,34] to investigate the interplay between orbital and spin currents in two series of heterostructures: YIG(40)/Pt(t_{Pt}) and YIG(40)/Pt(t_{Pt})/CuO_x(3), where $0 \leq t_{Pt} \leq 7$ nm. For the second series of samples, a Cu(3 nm) island with dimensions 1.5×2.0 mm^2 is deposited on top of the Pt layer. In this technique, illustrated in Fig. 3(a), a spin current is coherently injected through the YIG/Pt interface by the uniform precession of the YIG magnetization under FMR. The upward spin current density ($\vec{J}_S^{SP}$), diffuses through the Pt layer generating a local electric field, $\vec{E}_{ISHE} \propto \vec{J}_S^{SP} \times \hat{\sigma}$, by means of the ISHE, where spin current polarization $\hat{\sigma} \parallel \vec{M}_{YIG}$. By measuring the voltage difference (V_{SP}) produced between the two electrodes, we can define the SP signal as the current $I_{SP} = V_{SP}/R$, where R is the electric resistance along the Pt layer. Figure 3(b) shows typical I_{SP} signals for the sample YIG/Pt(2)CuO_x(3), which obey the equation $\vec{J}_C^{SP} = (2e/\hbar)\theta_{SH}(\vec{J}_S^{SP} \times \hat{\sigma})$ as expected, i.e., null at $\phi = 90°$ (black), maximum positive at $\phi = 0°$ (blue), and maximum negative $\phi = 180°$ (red). Here ϕ is the angle between the dc field and the direction of the voltage measurement. Inset of Fig. 3(b) shows the same behavior obtained for the sample YIG(40)/Pt(2).

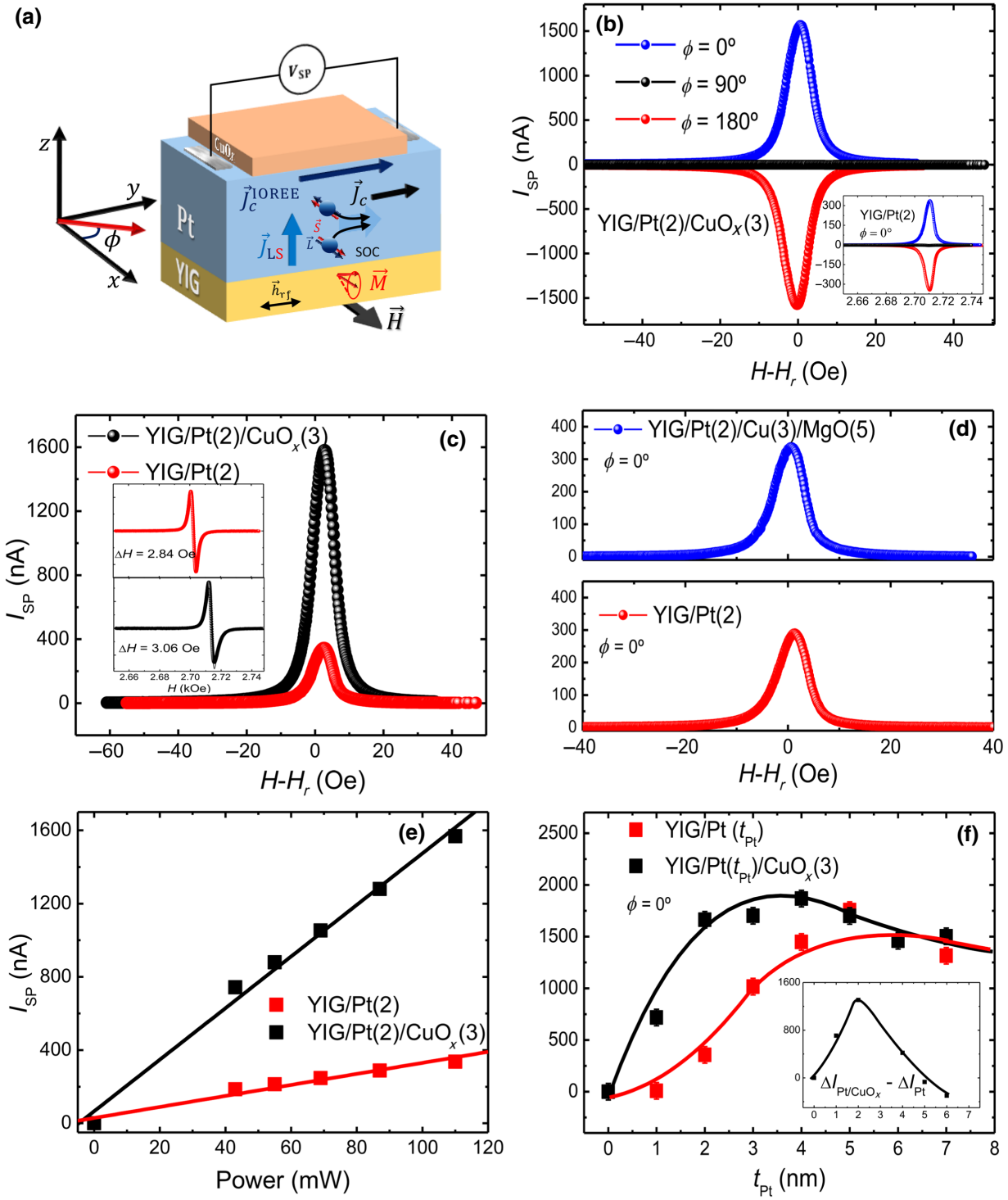

FIG. 3. (a) Schematically shows the SP configuration. (b) Typical I_{SP} signals for the samples with and without the CuO_x cover layer (inset). (c) Comparison of the SP signals of the samples with (black) and without (red) CuO_x capping layer, respectively, obtained for $P_{rf} = 110$ mW. The inset shows the derivative of the FMR absorption signal for both samples. (d) I_{SP} signals for samples YIG(40)/Pt(2)/Cu(3)/MgO(5) (blue) and YIG/Pt(2) (red), which confirm that the enhancement occurs only when the Cu cover layer is oxidized. (e) Dependence of I_{SP} signals, as a function of the rf power, for samples YIG/Pt(2) (red) and YIG/Pt(2)/CuO_x(3) (black). (f) Dependence of I_{SP} as a function of t_{Pt}, for samples YIG/Pt(2) (red) and YIG/Pt(2)/CuO_x(3) (black). The solid lines are guides to the eyes. The inset shows the difference between the data of the samples with and without the CuO_x cover layer, which reaches a maximum for $t_{Pt} \approx 2$ nm.

Figure 3(c) clearly shows the significant gain of the SP signal, for the sample YIG(40)/Pt(2)/CuO_x(3) (black) compared with the sample YIG(40)/Pt(2) (red).

While the bare YIG presented a FMR linewidth of $\Delta H = 2.63$ Oe, it increases to 2.84 Oe after deposition of Pt and increases for 3.06 Oe after deposition of CuO_x on top of Pt, which characterizes the transfer of spin angular moment from YIG to the Pt layer [inset of Fig. 3(c)]. To confirm the effect of the Cu oxidation, we prepare a sample in which the Cu layer is protected by a layer of MgO(5). The results of Fig. 3(d) show that the I_{SP} signals for samples YIG(40)/Pt(2)/Cu(3)/MgO(5) (blue) and YIG(40)/Pt(2) (red) are equivalent, thus confirming that the enhancement shown in Fig. 3(c) comes from the Pt(2)/CuO_x(3) interface. Figure 3(e) shows the dependence of the peak value of I_{SP}, as a function of the rf power used to excite the FMR, for both samples (see Appendix A). By comparing the slopes of the black and red lines, we observe that the gain in I_{SP}, due to the presence of CuO_x(3), is around 5 times. The dependence of I_{SP} as a function of the Pt layer thickness, with a rf power of 110 mW, for both sets of samples is shown in Fig. 3(f). The I_{SP} signal for the sample YIG(40)/Pt(t_{Pt}) (red) exhibits the usual behavior, i.e., increases as the t_{Pt} increases reaching the saturation for $t_{Pt} > 4$ nm. On the other hand, the dependence of I_{SP} on t_{Pt} for the set of samples with a capping layer of CuO_x(3) (black), increases sharply reaching a maximum at $t_{Pt} \sim 3$ nm, then decreases to the same range of saturation values observed for the YIG(40)/Pt(t_{Pt}) samples. The solid lines in Fig. 3(f) are guides to the eyes. The unusual dependence of I_{SP} on t_{Pt}, for the samples YIG(40)/Pt(t_{Pt})/CuO_x(3), is explained as due to the interplay between the spin and orbital states that is mediated by the strong SOC of Pt. The spin-orbital mixed current ($\vec{J}_{LS}$) is partially converted into charge current by means of the inverse spin and orbital Hall effects of Pt and by the strong IOREE at the Pt/CuO_x interface. As the Pt layer thickness increases, the $\vec{J}_{LS}$ current no longer reaches the Pt/CuO_x interface due to the finite diffusion length of the spin-orbital intertwined current in Pt, thus causing the measured voltage to decrease.

To confirm the results obtained by SP, we perform spin-injection measurements using the LSSE technique on the same two sets of samples. In LSSE, the application of a temperature gradient in a magnetic material generates a spin current along the direction of the temperature gradient, which is the magnetic analog of the thermoelectric Seebeck effect [35]. Figure 4(a) shows schematically the LSSE setup, in which a thermal gradient is applied perpendicular to the sample plane [see Appendix B]. It highlights the perpendicular temperature gradient $\vec{\nabla}T$ and the upward spin-orbital coupled current ($\vec{J}_{LS}$), the ISHE-like charge currents in Pt ($\vec{J}_C$) due to the inverse spin and orbital Hall effects, as well as the OREE current on the Pt/CuO_x interface.

Figure 4(b) shows LSSE signals, where thermal voltages (V_{LSSE}) are measured along sample plane for heterostructures of YIG(40)/Pt(2) (red) and YIG(40)/Pt(2)/CuO_x(3) (black). From negative to positive field sweep, the perpendicular temperature gradient is fixed at the same value for the measurements of both samples. Surprisingly, the measured LSSE signal value for the sample with a CuO_x capping layer increases more than 2 times compared to the sample without CuO_x. Figure 4(c) shows the LSSE signals of YIG(40)/Pt(2)/CuO_x(3) for various temperature differences ($0\ \text{K} \leq \Delta T \leq 20\ \text{K}$) between the heat baths placed on the lower and upper surfaces of the sample (see Appendix C). The LSSE signal amplitude (ΔI_{LSSE}), defined in Fig. 4(b), increases linearly as a function of ΔT, as summarized in Fig. 4(d) for the heterostructures of YIG(40)/Pt(2)/CuO_x(3) (black) and YIG(40)/Pt(2) (red), respectively. The linear fits of Fig. 4(d) are obtained by means of $\Delta I_{LSSE} = -\xi \Delta T \cos\phi$ [36], where $\xi = (S_{FM}/R)(w_{Pt}/t_{YIG} + t_{GGG})$ (see Appendix C). Here, S_{FM} is the spin-Seebeck coefficient, w_{Pt} is the distance between the electrical contacts, ϕ is the azimuthal angle as defined in Fig. 4(a), and t_{YIG} and t_{GGG} are the thicknesses of the YIG and GGG layers, respectively. From the linear fits shown in Fig. 4(d) we obtain $\xi^{(1)}/\xi^{(2)} \cong 2.6$, where $\xi^{(1)}$ and $\xi^{(2)}$ are the linear coefficients for the black and red lines, respectively. Thus, the presence of CuO_x increases the LSSE signal by a factor of 2.6. Figures 4(e) and 4(f) show the dependence of ΔI_{LSSE} for both series of samples as a function of t_{Pt} for $\Delta T = 27$ K and $\Delta T = 3$ K, respectively. As expected, the dependence of $\Delta I_{LSSE} \times t_{Pt}$ for YIG(40)/Pt(t_{Pt}) is given by $\Delta I_{LSSE} = \beta \lambda_N \tanh(t_{Pt}/2\lambda_N)$, where β depends on the interface YIG/Pt properties and λ_N is the spin-diffusion length in the Pt layer [37]. ΔI_{LSSE} increases monotonically, reaching the saturation for $t_{Pt} > 4$ nm, and the red line corresponds to the best fit to the data with $\lambda_N = 1.6 \pm 0.2$ nm, which is in the range of reported spin-diffusion lengths for Pt that span an order of magnitude, ranging from just over 1 to 10 nm [34,38]. On the other hand, the results for the samples YIG(40)/Pt(t_{Pt})/CuO_x(3), indicated in Figs. 4(e) and 4(f) by the black symbols, shows the same behavior of the SP signal of Fig. 3(f). Black lines are guides to the eyes. The LSSE signal rapidly increases as a function of t_{Pt}, reaches a maximum for $t_{Pt} \approx 3$ nm and then decreases to values of the same order as the saturation values obtained for the YIG(40)/Pt(t_{Pt}) samples.

This very peculiar behavior can also be explained as being due to the interplay between the electron spin and orbital degrees of freedom. In the LSSE, an upward spin current, $\vec{J}_S^{LSSE} \parallel \vec{\nabla}_z T$, driven by the $\vec{\nabla}_z T$, is injected through the YIG/Pt interface. Due to the strong SOC of Pt, the out-of-equilibrium spin states, thermally pumped into Pt, give rise to a spin-orbital mixed current ($\vec{J}_{LS}$). As the coupled spin-orbital current propagates upward through the Pt layer, it is converted into charge current, either by

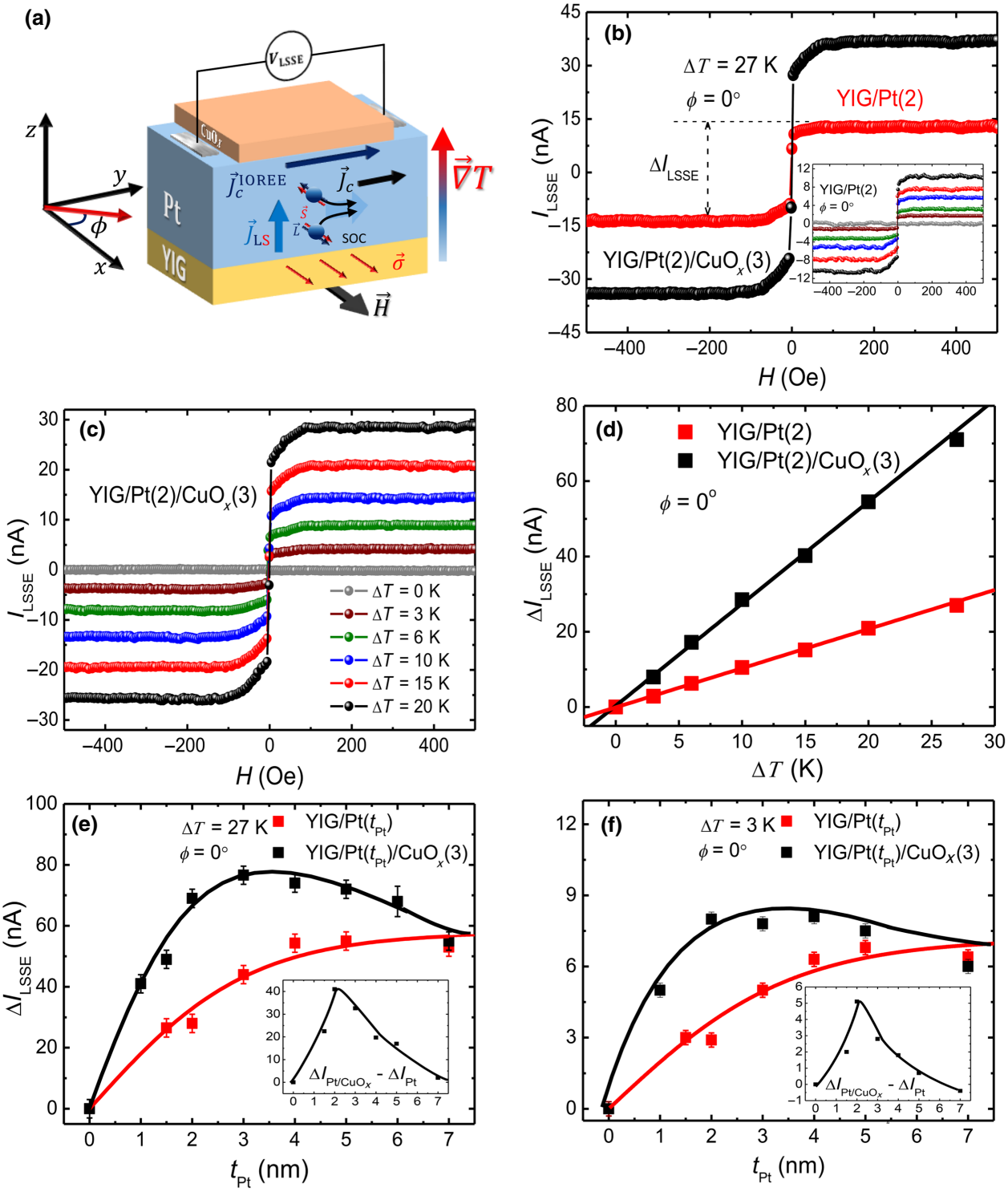

FIG. 4. (a) Schematically shows the LSSE configuration. (b) Field sweep of the LSSE signal for the samples with (black) and without (red) a capping layer of $CuO_x(3)$, for $\Delta T = 27$ K. With the deposition of the CuO_x layer, the LSSE signal obtained a gain of order 2.6. (c) Field scan curves for values of ΔT ranging from 0 to 20 K, for the sample with the cover layer of CuO_x. The inset of (b) shows the same curves obtained for sample YIG(40)/Pt(2). (d) Dependence of ΔI_{LSSE} as a function of ΔT for samples YIG/Pt(2)/CuO_x(3) (black) and YIG/Pt(2) (red), where ΔI_{LSSE} is defined in (b). (e),(f) Dependence of ΔI_{LSSE} as a function of t_{Pt} for $\Delta T = 27$ K and $\Delta T = 3$ K, respectively. The red symbols are the data for the sample YIG/Pt(t_{Pt}) and the black symbols are the data for the sample with the capping layer of CuO_x. The insets of (e),(f) show the difference between the data of the samples with and without the CuO_x cover layer, which reaches a maximum for $t_{Pt} \approx 2$ nm.

the inverse SHE or inverse OHE, as well as by the strong OREE at the Pt/CuO_x interface. It is wortwhile to mention that preliminary results performed in YIG/Pt(4)/AlO_x(3) also exhibit a gain of more than twice compared to YIG/Pt(4) (see Fig. 8,Appendix C).

The interaction between charge, spin, and orbital degrees of freedom, triggered by the FMR-driven or thermal-driven spin pumping, represents a unifying principle to explain the experimental results reported in this work. By injecting the pure spin current from the FMR SP or LSSE from YIG into Pt, the nonequilibrium electronic states have strong intertwining between the spin and orbital and carries spin-orbital mixed current. In Pt, a part of the spin-orbital mixed current is converted into charge current. This occurs either by the inverse SHE or inverse OHE. We note that this has been conventionally interpreted solely in terms of the inverse SHE, neglecting the orbital contribution. Meanwhile, as the spin-orbital coupled current propagates across the Pt layer and reaches the CuO_x interface, it is converted to charge current via the inverse OREE. However, if the Pt layer is thicker than the relaxation length for the spin-orbital mixed current, it cannot reach the CuO_x interface and only the inverse SHE and OHE contributions contribute. This explains why the efficiencies for YIG/Pt and YIG/Pt/CuO_x converge to the same value for $t_{Pt} > 7$ nm.

In conclusion, we use LSSE and FMR SP techniques to investigate the interplay between spin, orbital, and charge degrees of freedom in heterostructures of YIG(40)/Pt(t_{Pt})/CuO_x(3). Due to the strong SOC of Pt, the spin states, pumped through the YIG/Pt interface, couple with the local orbital states, thus generating an upward pure spin-orbital current ($\vec{J}_{LS}$) without flow of charge. Part of this current is converted, within the Pt, into a transverse charge current by either the inverse-SHE effect or the inverse-OHE effect. Part of the remaining spin-orbital current that flows upward, is transformed into a transverse charge current by means of the inverse OREE. This current is added to the previous charge current, thus increasing the resulting charge current. The dependence of the charge current as a function of Pt-layer thickness, provides a clear picture of the phenomenon of converting spin-orbital current to charge current. As the Pt-layer thickness becomes larger than the spin-orbital diffusion length, the $\vec{J}_{LS}$ no longer reaches the Pt/CuO_x interface, and the IOREE mechanism ceases to occur. Therefore, the charge-current value is reduced to the saturation values of the charge currents generated only by the inverse SHE combined with the inverse OHE. Certainly, the results reported here open different avenues to understand the basic mechanisms underlying the spin-orbital coupling phenomena.

All data are included in the submitted material.

ACKNOWLEDGMENTS

This research is supported by Conselho Nacional de Desenvolvimento Científico e Tecnológico (CNPq), Coordenação de Aperfeiçoamento de Pessoal de Nível Superior (CAPES) (Grant No. 0041/2022), Financiadora de Estudos e Projetos (FINEP), Fundação de Amparo à Ciência e Tecnologia do Estado de Pernambuco (FACEPE), Universidade Federal de Pernambuco, Multiuser Laboratory Facilities of DF-UFPE, and Fundação de Amparo à Pesquisa do Estado de Minas Gerais (FAPEMIG) - Rede de Pesquisa em Materiais 2D and Rede de Nanomagnetismo. D.G and Y.M. acknowledge support by the Deutsche Forschungsgemeinschaft (DFG, German Research Foundation) - TRR 173/2 - 268565370 (project A11).

CONFLICT OF INTEREST

The authors declare no competing interest.

APPENDIX A: SAMPLE PREPARATION AND SPIN-PUMPING MEASUREMENTS

To carry out this work we produce YIG(40)/Pt(t)/CuO_x(3) and YIG(40)/Pt(t_{Pt}) heterostructures, where t_{Pt}

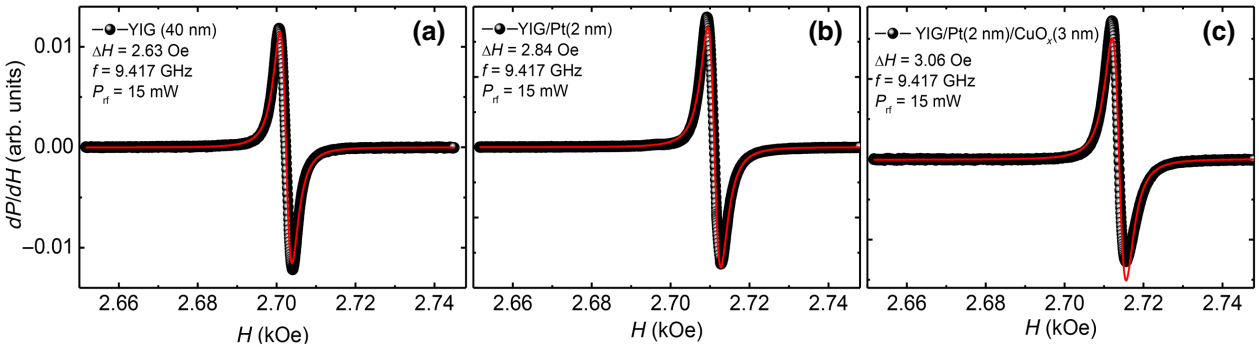

FIG. 5. Ferromagnetic resonance measurements for samples of (a) pure YIG, (b) YIG/Pt (2 nm), and (c) YIG/Pt(2 nm)/CuO_x(3 nm), with a layer of Cu(3 nm) that is left to oxidize naturally for 2 days. The curve in red is the fit of the FMR from the derivative of a Lorentzian curve.

ranges from 1 to 7 nm. The YIG samples consist of single-crystal yttrium iron garnet (111) films grown by liquid phase epitaxy (LPE) onto a 0.5-mm-thick (111)-oriented $Gd_3Ga_5O_{12}$ (GGG) substrates. In the LPE, the films are grown by the precipitation of a crystalline film from a supersaturated melt in which Y_2O_3 and Fe_2O_3 are added to a flux of $P_bO + B_2O_3$. The quality of the YIG samples is attested by the small FMR linewidth, which is 2.63 Oe [see Fig. 5(a)]. The investigated samples are rectangular pieces with dimensions of 3.0×1.5 mm^2 cut from the same single-crystal YIG wafer with thickness around 40 nm. The metal films are dc-sputter-deposited at room temperature in a 3-mTorr argon atmosphere in the sputter-up configuration, with the substrate placed 9 cm from the target, and with the following deposition rates: 10.2 nm/min for Pt and 13.2 nm/min for Cu. The base pressure is 2.0×10^{-7} Torr and a 5-min presputtering procedure is used to clean the targets.

For FMR and spin-pumping measurements, the sample is mounted on one end of a PVC rod that is inserted through a hole drilled in the center of the back wall of a rectangular microwave cavity operating in the transverse electric (TE_{102}) mode, at a frequency of 9.41 GHz with a Q factor around 2000. The sample is slightly inserted into the cavity in the plane of the back wall, in a position of maximum rf magnetic field and minimum rf electric field to avoid the generation of galvanic effects driven by the rf electric field. With this arrangement, the static magnetic field H, and the microwave field h_{rf} are in the film plane and kept perpendicular to each other as the sample is rotated for the measurements of the angular dependence of the FMR spectra and the dc voltage induced by the spin-to-charge conversion. Field scan spectra of the derivative of the microwave absorption dP/dH are obtained by modulating the field at 1.2 kHz and using lock-in detection. Figures 5(b) and 5(c) show the FMR absorption spectra of the YIG layer in contact with the Pt film and Pt/CuO_x measured with microwave power of 15 mW. From the FMR spectra in Fig. 5 we obtain the values of the half-width at half-maximum (HWHM) linewidth for YIG/Pt [Fig. 5(b)] and YIG/Pt/CuO_x [Fig. 5(c)], respectively, 2.84 and 3.06 Oe, which are larger than 2.63 Oe for single bare YIG [Fig. 5(a)]. In this case, the atomic contact of the YIG layer with the Pt film and Pt/CuO_x produces an additional damping due to the spin-pumping process.

APPENDIX B: LSSE MEASUREMENT

The detection of the LSSE signals is performed by measuring an electrical voltage that arises in the nonmagnetic metal, due to the conversion of the injected pure spin-orbital current into a charge current by the ISHE including spin and orbital components. The application of a perpendicular thermal gradient in the ferromagnetic/nonmagnetic (FM/NM) bilayer generates an upward collective, noncoherent excitation of the YIG spins. The accumulation of spins at the FM/NM interface diffuses noncoherently through the NM, with a characteristic penetration length (λ_{LS}). To observe the LSSE, the samples are placed with the GGG substrate side in contact with a copper plate that functions as a thermal bath at room temperature, while the top of the sample is in thermal contact with a commercial 2×2 mm^2 Peltier module, responsible for creating the temperature gradient across the sample. To ensure a better heat flow through the heterostructure, both interfaces are glued with thermal paste, and the temperature difference ($\Delta T = [T_Q - T_A]$) between the top and the bottom surfaces measured using two thermocouples. The ISHE and IOHE voltage is directly measured between two electrodes made with silver ink at the ends of the Pt film, as schematically shown in Fig. 6(a). Figure 6(b) shows the dependence of the temperature difference, between the top and bottom surfaces, as a function of the dc electric current applied to the Peltier module.

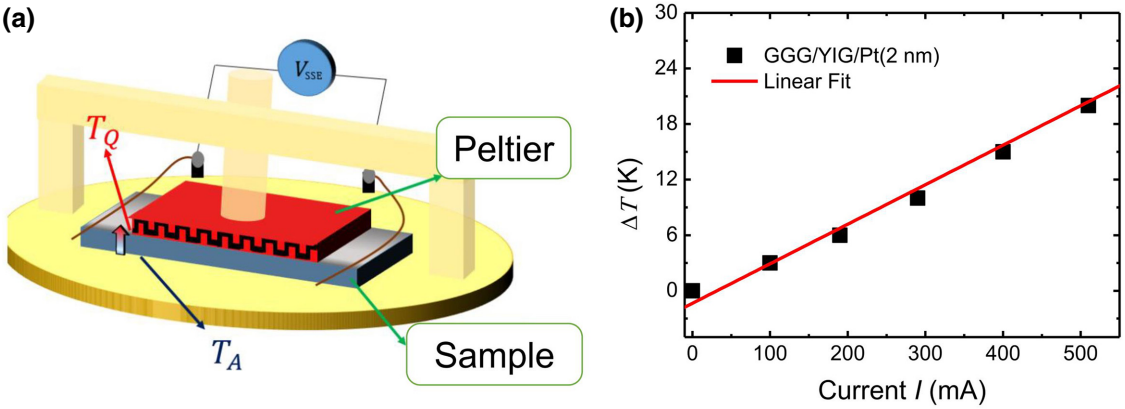

FIG. 6. (a) Schematic of the assembly used to measure the LSSE. (b) Thermal gradient ΔT as a function of electric current applied to the Peltier module.

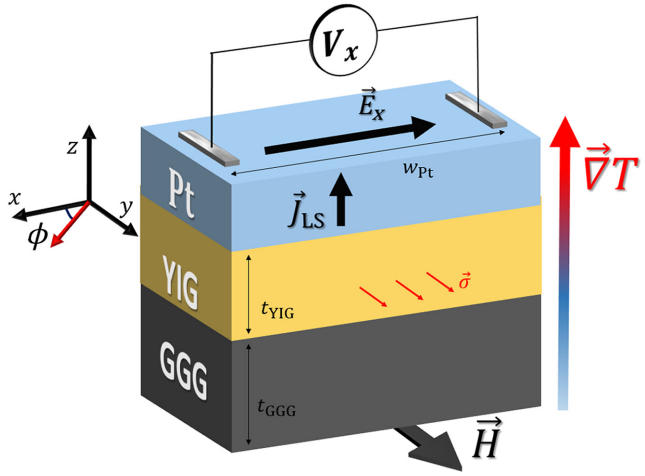

FIG. 7. Schematic illustration of the LSSE in a heterostructure of GGG, YIG, and Pt.

APPENDIX C: SPIN SEEBECK COEFFICIENT

The LSSE plays a role in the spintronics scenario as a potential source of a thermally generated spin current. The LSSE appears in a ferrimagnetic insulator, which in most experiments uses YIG films, subjected to a perpendicular temperature gradient. Because of the magnetic moment carried by out-of-equilibrium magnons, a spin current flows parallel to the direction of the temperature gradient and is injected into a layer of a nonmagnetic metallic material with strong SOC. Due to ISHE and IOHE this $\vec{J}_{LS}$ current is converted into a charge current, which leads to the emergence of an electric field given by $\vec{E} \propto (\vec{J}_{LS} \times \hat{\sigma})$, where $\hat{\sigma}$ is the spin polarization vector. According to Fig. 7 the electric field is along the x direction and can be written as $E_x = S_{FM}\nabla_z T$ [39–41], where S_{FM} is the spin Seebeck coefficient with unit of V/K. Still according to Fig. 7 the electric potential difference is given by $\Delta V_x = E_x w_{NM} \cos\phi$. Defining $\nabla_z T = \Delta T_z / t_{FM}$, the potential difference due to LSSE becomes $\Delta V_x = S_{FM}(w_{NM}/t_{FM})\Delta T_z \cos\phi$. However, it is worthwhile to consider the thermal conductivity (κ) along the sample and the thickness of the substrate and the FM layer as the temperature difference applied to the sample is not equal to the temperature difference in the FM [40,41]. Considering the substrate as the GGG and the FM layer as the YIG, we can make $\kappa_{GGG} \approx \kappa_{YIG}$ [42,43] neglecting the interfacial resistances, the potential difference measured between the ends of the sample becomes [41] $\Delta V_x = S_{FM}(w_{Pt}/t_{YIG} + t_{GGG})\Delta T_z \cos\phi$.

It is more convenient to express the electric current as a function of temperature, that is, $\Delta I_{LSSE} = \xi \Delta T_Z \cos\phi$, with $\xi = (S_{FM}/R)(w_{Pt}/t_{YIG} + t_{GGG})$. For $\phi = 0°$, from the linear fit of the data presented in Fig. 4(d), we find $\xi_1 = (2.64 \pm 0.04)$ nA/K for the sample with the Cu layer; and $\xi_2 = (1.01 \pm 0.02)$ nA/K for the sample without the Cu layer. Using $R_1 = 438\ \Omega$, $R_2 = 385\ \Omega$, $w_{Pt} = 3$ mm, $t_{YIG} = 40$ nm, $t_{GGG} = 0.5$ mm, and $\phi = 0°$, we find $S^{(1)}_{FM} = (0.20 \pm 0.02)\ \mu$V/K and $S^{(2)}_{FM} = (0.07 \pm 0.02)\ \mu$V/K, and the ratio of the coefficients is $S^{(1)}_{FM}/S^{(2)}_{FM} = 2.85$.

APPENDIX D: ADDITIONAL COMMENTS

Additional remarks on the interpretation of our results are necessary at this point. After detailed analysis of all possible physical mechanisms to explain our results, the IOREE proved to be the most reliable to elucidate the large increase in the SP and LSSE observed signals. It is useful to recall that our result is the inverse effect of the effect investigated in Ref. [29], but the basic mechanism to explain both phenomena is essentially the same. Both works investigate the role played by the Pt/CuO_x interface in the interplay between spin current and orbital current, where the oxidation of the Cu(3 nm) layer is obtained by the same procedure (2 days in ambient atmosphere). The nonmonotonic behavior of the SOT efficiency, shown in Fig. 2 of Ref. [29], is like the voltage behavior measured in our work [Figs. 3(f) and 4(f)]. Therefore, the signal enhancement is due to the additional charge current driven by the IOREE that occurs at the Pt/CuO_x upper interface. The large SOC of Pt plays a crucial role in the spin and orbital mixed upflow, which explains the IOREE occurring at the upper Pt/CuO_x interface. Emphasizing, in our experiment we are injecting an upward-flowing spin current, while in the experiment reported in Ref. [29] the authors inject a charge current at the Pt/CuO_x. The spin-vorticity mechanism discussed in Ref. [31], is ruled out because, to be effective, this mechanism needs an oxidation gradient along the CuO_x layer, which does not occur in thin films of

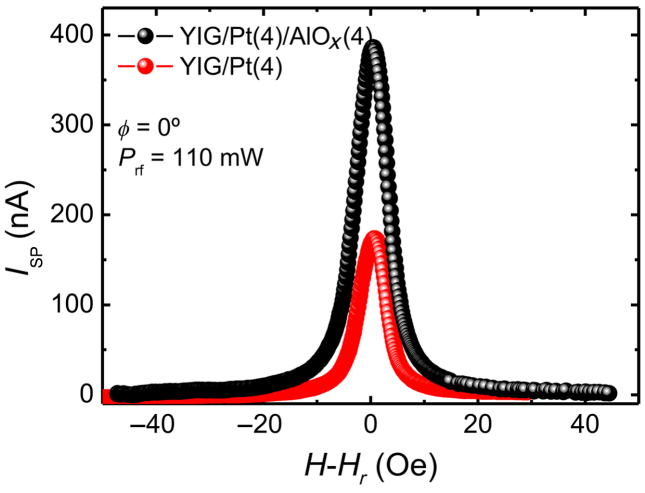

FIG. 8. Gain in the spin-pumping signal driven by the Pt/AlO_x interface of YIG/Pt(4 nm)/AlO_x(3 nm) (black) in comparison to YIG/Pt(4 nm) (red). Measurements are performed with a power of 100 mW and $\phi = 0°$.

CuO_x(3 nm). In addition, we presume that Ref. [31] is not successful to detect the IOREE, because the authors use the Cu/CuO_x interface instead of the Pt/CuO_x interface. The large SOC material is missing in the Cu/CuO_x structure, so in this system the spin-orbital current is negligible. Furthermore, we investigate samples of YIG/Pt(4 nm) and YIG/Pt(4 nm)/AlO_x(3 nm), where the Al layer is left to naturally oxidize, and also find a significant increase in the SP signal as seen in Fig. 8. This preliminary result confirms that IOREE can occur at interfaces of Pt with other light metal oxides. Certainly, alternative studies related to the role played by different oxide interfaces need to be investigated more systematically, and we believe that our investigation will motivate future works.

[1] B. Dieny, *et al.*, Opportunities and challenges for spintronics in the microelectronics industry, Nat. Electron. **3**, 446 (2020).

[2] A. Hirohata, K. Yamada, Y. Nakatani, I. L. Prejbeanu, B. Diény, P. Pirro, and B. Hillebrands, Review on spintronics: Principles and device applications, J. Magn. Magn. Mater. **509**, 166711 (2020).

[3] M. I. Dyakonov and V. I. Perel, Current-induced Spin Orientation of Electrons in Semiconductors, Phys. Rev. Lett. A **35**, 459 (1971).

[4] J. E. Hirsch, Spin Hall Effect, Phys. Rev. Lett. **83**, 1834 (1999).

[5] J. Sinova, S. O. Valenzuela, J. Wunderlich, C. H. Back, and T. Jungwirth, Spin Hall effects, Rev. Mod. Phys. **87**, 1213 (2015).

[6] Yu. A. Bychkov and É. I. Rashba, Properties of a 2D electron gas with lifted spectral degeneracy, JETP Lett. **39**, 66 (1984).

[7] V. M. Edelstein, Spin polarization of conduction electrons induced by electric current in two-dimensional asymmetric electron systems, Solid State Commun. **73**, 233 (1990).

[8] J. C. Rojas Sánchez, L. Vila, G. Desfonds, S. Gambarelli, J. P. Attané, J. M. De Teresa, C. Magén, and A. Fert, Spin-to-charge conversion using Rashba coupling at the interface between non-magnetic materials, Nat. Commun. **4**, 2944 (2013).

[9] A. Manchon, H. C. Koo, J. Nitta, S. M. Frolov, and R. A. Duine, New perspectives for Rashba spin–orbit coupling, Nat. Mater. **14**, 871 (2015).

[10] I. Mihai Miron, K. Garello, G. Gaudin, P.-J. Zermatten, M. V. Costache, S. Auffret, S. Bandiera, B. Rodmacq, A. Schuhl, and P. Gambardella, Perpendicular switching of a single ferromagnetic layer induced by in-plane current injection, Nature **476**, 189 (2011).

[11] H. L. Wang, C. H. Du, Y. Pu, R. Adur, P. C. Hammel, and F. Y. Yang, Scaling of Spin Hall Angle in 3d, 4d, and 5d Metals from $Y_3Fe_5O_{12}$/Metal Spin Pumping, Phys. Rev. Lett. **112**, 197201 (2014).

[12] Q. Shao, P. Li, L. Liu, H. Yang, S. Fukami, A. Razavi, H. Wu, K. Wang, F. Freimuth, Y. Mokrousov, *et al.*, Roadmap of spin–orbit torques, IEEE Trans. Magn. **57**, 800439 (2021).

[13] H. An, Y. Kageyama, Y. Kanno, N. Enishi, and K. Ando, Spin–torque generator engineered by natural oxidation of Cu, Nat. Commun. **7**, 13069 (2016).

[14] K. Hasegawa, Y. Hibino, M. Suzuki, T. Koyama, and D. Chiba, Enhancement of spin-orbit torque by inserting CoO_x layer into Co/Pt interface, Phys. Rev. B **98**, 020405 (2018).

[15] Y. Kageyama, Y. Tazaki, H. An, T. Harumoto, T. Gao, H. Shi, and Kazuya Ando, Spin-orbit torque manipulated by fine-tuning of oxygen-induced orbital hybridization, Sci. Adv. **5**, eaax4278 (2019).

[16] J. Kim, D. Go, H. Tsai, D. Jo, K. Kondou, H.-W. Lee, and YoshiChika Otani, Nontrivial torque generation by orbital angular momentum injection in ferromagnetic-metal/Cu/Al_2O_3 trilayers, Phys. Rev. B **103**, L020407 (2021).

[17] B. Andrei Bernevig, T. L. Hughes, and Shou-Cheng Zhang, Orbitronics: The Intrinsic Orbital Current in p-Doped Silicon, Phys. Rev. Lett. **95**, 066601 (2005).

[18] H. Kontani, T. Tanaka, D. S. Hirashima, K. Yamada, and J. Inoue, Giant Orbital Hall Effect in Transition Metals: Origin of Large Spin and Anomalous Hall Effects, Phys. Rev. Lett. **102**, 016601 (2009).

[19] D. Go, D. Jo, C. Kim, and Hyun-Woo Lee, Intrinsic Spin and Orbital Hall Effects from Orbital Texture, Phys. Rev. Lett. **121**, 086602 (2018).

[20] D. Jo, D. Go, and Hyun-Woo Lee, Gigantic intrinsic orbital Hall effects in weakly spin-orbit coupled metals, Phys. Rev. B **98**, 214405 (2018).

[21] D. Go, D. Jo, Hyun-Woo Lee, M. Kläui, and Y. Mokrousov, Orbitronics: Orbital currents in solids, EPL **135**, 37001 (2021).

[22] S. R. Park, C. H. Kim, J. Yu, J. H. Han, and C. Kim, Orbital-Angular-Momentum Based Origin of Rashba-Type Surface Band Splitting, Phys. Rev. Lett. **107**, 156803 (2011).

[23] J.-H. Park, C. H. Kim, Hyun-Woo Lee, and J. H. Han, Orbital chirality and Rashba interaction in magnetic bands, Phys. Rev. B **87**, 041301(R) (2013).

[24] J.-H. Park, C. H. Kim, J.-W. Rhim, and J. H. Han, Orbital Rashba effect and its detection by circular dichroism angle-resolved photoemission spectroscopy, Phys. Rev. B **85**, 195401 (2012).

[25] D. Go and Hyun-Woo Lee, Orbital torque: Torque generation by orbital current injection, Phys. Rev. Res. **2**, 013177 (2020).

[26] D. Go, J.-P. Hanke, P. M. Buhl, F. Freimuth, G. Bihlmayer, Hyun-Woo Lee, Y. Mokrousov, and S. Blügel, Toward surface orbitronics: giant orbital magnetism from the orbital Rashba effect at the surface of sp-metals, Sci. Rep. **7**, 46742 (2017).

[27] D. Go, D. Jo, T. Gao, K. Ando, S. Blügel, Hyun-Woo Lee, and Y. Mokrousov, Orbital Rashba effect in a surface-oxidized Cu film, Phys. Rev. B **103**, L121113 (2021).

[28] L. Salemi, M. Berritta, A. K. Nandy, and P. M. Oppeneer, Orbitally dominated Rashba-Edelstein effect in noncentrosymmetric antiferromagnets, Nat. Commun. **10**, 5381 (2019).

[29] S. Ding, A. Ross, D. Go, L. Baldrati, Z. Ren, F. Freimuth, S. Becker, F. Kammerbauer, J. Yang, G. Jakob, *et al.*, Harnessing Orbital-to-Spin Conversion of Interfacial Orbital Currents for Efficient Spin-Orbit Torques, Phys. Rev. Lett. **125**, 177201 (2020).

[30] Y. Tazaki, Y. Kageyama, H. Hayashi, T. Harumoto, T. Gao, J. Shi, and K. Ando, Current-induced torque originating from orbital current, arXiv:2004.09165.

[31] G. Okano, M. Matsuo, Y. Ohnuma, S. Maekawa, and Y. Nozaki, Nonreciprocal Spin Current Generation in Surface-Oxidized Copper Films, Phys. Rev. Lett. **122**, 217701 (2019).

[32] A. A. Dubale, C.-J. Pan, A. G. Tamirat, H.-M. Chen, W.-N. Su, C.-H. Chen, J. Rick, D. W. Ayele, B. A. Aragaw, J.-F. Lee, Y.-W. Yang, and B.-J. Hwang, Heterostructured Cu_2O/CuO decorated with nickel as a highly efficient photocathode for photoelectrochemical water reduction, J. Mater. Chem. A **3**, 12482 (2015).

[33] Y. Tserkovnyak, A. Brataas, and G. E. W. Bauer, Enhanced Gilbert Damping in Thin Ferromagnetic Films, Phys. Rev. Lett. **88**, 117601 (2002).

[34] A. Azevedo, L. H. Vilela-Leão, R. L. Rodríguez-Suárez, A. F. Lacerda Santos, and S. M. Rezende, Spin pumping and anisotropic magnetoresistance voltages in magnetic bilayers: Theory and experiment, Phys. Rev. B **83**, 144402 (2011).

[35] K. Uchida, S. Takahashi, K. Harii, J. Ieda, W. Koshibae, K. Ando, S. Maekawa, and E. Saitoh, Observation of the spin Seebeck effect, Nature **455**, 778 (2008).

[36] S. M. Rezende, R. L. Rodríguez-Suárez, R. O. Cunha, A. R. Rodrigues, F. L. A. Machado, G. A. Fonseca Guerra, J. C. Lopez Ortiz, and A. Azevedo, Magnon spin-current theory for the longitudinal spin-Seebeck effect, Phys. Rev. B **89**, 014416 (2014).

[37] Kuntal Roy, Estimating the spin diffusion length and the spin Hall angle from spin pumping induced inverse spin Hall voltages, Phys. Rev. B **96**, 174432 (2017).

[38] Luqiao Liu, R. A. Buhrman, and D. C. Ralph, Review and analysis of measurements of the spin Hall effect in platinum, arXiv:1111.3702.

[39] C. M. Jaworski, J. Yang, S. Mack, D. D. Awschalom, J. P. Heremans, and R. C. Myers, Observation of the spin-Seebeck effect in a ferromagnetic semiconductor, Nat. Mater. **9**, 898 (2010).

[40] A. Sola, M. Kuepferling, V. Basso, M. Pasquale, T. Kikkawa, K. Uchida, and E. Saitoh, Evaluation of thermal gradients in longitudinal spin Seebeck effect measurements, J. Appl. Phys. **117**, 17C510 (2015).

[41] P. Jiménez-Cavero, I. Lucas, D. Bugallo, C. López-Bueno, R. Ramos, P. A. Algarabel, M. R. Ibarra, F. Rivadulla, and L. Morellón, Quantification of the interfacial and bulk contributions to the longitudinal spin Seebeck effect, Appl. Phys. Lett. **118**, 092404 (2021).

[42] B. Lüthi, Thermal conductivity of yttrium iron garnet, J. Phys. Chem. Solids **23**, 35 (1962).

[43] J. Ahn, Thermal and optical properties of gadolinium gallium garnet, Mater. Res. Bull. **17**, 1393 (1982).